Available online at www.sciencedirect.com
ScienceDirect
Journal of Sound and Vibration 311 (2008) 20–38
JOURNAL OF SOUND AND VIBRATION
www.elsevier.com/locate/jsvi

Internal chamber modeling of a solid rocket motor: Effects of coupled structural and acoustic oscillations on combustion

John Montesano, Kamran Behdinan*, David R. Greatrix, Zouheir Fawaz

Department of Aerospace Engineering, Ryerson University, Toronto, Canada M5B 2K3

Received 6 June 2005; received in revised form 13 August 2007; accepted 16 August 2007
Available online 22 October 2007

Abstract

This paper outlines modeling considerations for the internal ballistics of solid rocket motors. The simulation model consists of three coupled physical components, including the combined propellant and motor structure, the core fluid flow and the propellant combustion. A coupling component is also employed to control the fluid–structure–combustion interaction during the simulations. The results of simulating a motor firing illustrate the coupled effects of the structural and acoustic oscillations with the combustion model. Comparisons of the predicted results with experimental test results indicate a good correlation exists, providing support for the present simulation model.

1. Introduction

In the aerospace industry, fluid–structure interaction-type problems commonly arise and are more likely to be analysed with present-day advancements in computation technology. Some typical examples found in the industry are of aircraft wing flutter, aero-acoustic-type problems and pipe flows, to mention a few. In the present study, the internal chamber modeling of a solid rocket motor (SRM) is considered. This particular application does not represent a traditional fluid–structure interaction problem, mainly due to the complexity of the combustion process in the SRM chamber.

Over the past few decades, various attempts have been made to accurately model the internal ballistics in the chamber of an SRM. Gottlieb and Greatrix [1] employed a one-dimensional flow model, incorporated with an erosive burning model and an empirical pressure-based burning law that represented the combustion model. The propellant burning was solved in conjunction with the flow equations, but there was no structural influence on the combustion and flow model components. Later, work by Greatrix [2,3] and Greatrix and Harris [4] attempted to include the effects of the surrounding motor structure's radial and axial vibration on the internal flow and combustion. It was shown that the surrounding structure plays a significant role in altering the combustion behaviour of the propellant grain. This finding is consistent with experimental motor firings that suggest that the structural acceleration field augments the propellant combustion [5].

*Corresponding author. Tel.: +1 416 979 5000x6414; fax: +1 416 979 5056.
E-mail address: kbehdina@ryerson.ca (K. Behdinan).

0022-460X/$ - see front matter
doi:10.1016/j.jsv.2007.08.030

Nomenclature

a_l	propellant axial acceleration, m/s^2
a_n	propellant normal acceleration, m/s^2
A	local core area, m^2
$\vec{B}$	propellant regression vector, m
C_p	gas specific heat capacity, J/kg K
C_s	propellant specific heat, J/kg K
$[C]$	structural damping matrix, kg/s
d	local port hydraulic diameter, m
E	structural modulus, Pa or gas total specific energy, J/kg
$\{F\}$	structural external force vector, N
G_a	accelerative mass flux, kg/s m^2
h	convective heat transfer coefficient, W/m^2 K
$[K]$	structural stiffness matrix, N/m
$[M]$	structural mass matrix, kg
p	local static pressure, Pa
r_b	overall burn rate, m/s
r_0	base burn rate, m/s
t	time, s
T_f	flame temperature, K
T_s	propellant surface temperature, K
u	local flow axial velocity, m/s
$\{u\}$	nodal displacement vector, m
γ	gas specific heat ratio
ΔH_s	net surface heat of reaction, J/kg
Δt	time step, s
ζ	structural damping ratio
κ	port radial dilatation, s^{-1}
v	Poisson's ratio
ρ	local gas density or solid density, kg/m^3
ρ_s	propellant density, kg/m^3
ϕ_d	augmentation orientation angle, rad
ω_n	structural natural frequency, Hz

More recently, Loncaric et al. [6] attempted to model the internal ballistics for a star-grain SRM. The effect of the structural acceleration field on the combustion of the propellant was illustrated using a two-dimensional structural model.

Other researchers [7,8] have also attempted to model the structural vibrations of the motor and couple them with the internal flow and propellant combustion, employing an adaptive structural mesh compensating for regression of the propellant structure. It is the main objective of this study to accurately model the nonlinear unsteady fluid–structure–combustion (FSC) interaction occurring in the combustion chamber of an SRM. The detail of each simulation model component is presented, as is the implementation of the coupled algorithm. Also, numerical simulations of this study (involving a sleeved cylindrical-grain SRM subjected to a pressure-pulse disturbance initiated within the flow) are presented and compared with experimental results. The structural response and acoustic oscillations caused by the disturbance and its effects on the burning rate are evaluated in an attempt to yield a better understanding of the physical phenomena inherent to SRM internal ballistic flow (IBF).

2. Modeling considerations

The numerical model consists of three main components: the structural finite element (FE) component, the IBF component and the combustion (or burning rate) component. Each model component is developed in a FORTRAN 90 algorithm, as is the coupling algorithm used to control the simulation.

2.1. Structural component

A schematic of a typical sleeved cylindrical-grain motor structure is included in Fig. 1, with the steel static-test sleeve, the aluminium casing (including the head-end plate and nozzle structure) and the propellant grain indicated in the figure. For this study, the material properties and geometry used for the reference cylindrical-grain motor are given in Table 1, and are for a small test motor configuration. The motor structure is represented by a three-dimensional model in order to account for any axial and transverse motion during a simulated motor firing. The head-end structure is modeled as a flat-plate acting as an end-cap to the aluminium casing. In this study, detailed modeling of the nozzle structure is omitted for simplicity (the nozzle is treated as a rigid structure). The nozzle structure does not influence the propellant grain motion to a large

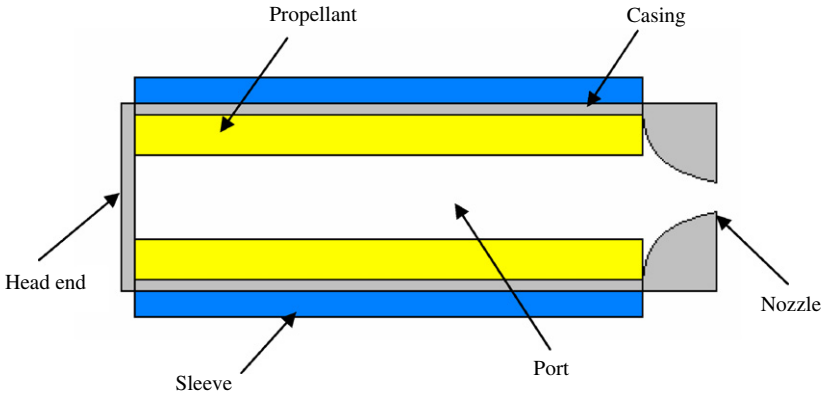

Fig. 1. Cylindrical-grain SRM schematic.

Table 1
Reference cylindrical SRM structural properties

Steel modulus (E_{st})	200 GPa
Steel Poisson's ratio (ν_{st})	0.3
Steel density (ρ_{st})	7850 kg/m^3
Steel inner wall radius (r_{st})	33.67 mm
Steel thickness (t_{st})	4.67 mm
Aluminium modulus (E_{al})	80 GPa
Aluminium Poisson's ratio (ν_{al})	0.33
Aluminium density (ρ_{al})	2700 kg/m^3
Aluminium inner wall radius (r_{al})	32.4 mm
Aluminium thickness (t_{al})	1.27 mm
Propellant modulus (E_s)	0.045 GPa
Propellant Poisson's ratio (ν_s)	0.497
Propellant density (ρ_s)	1730 kg/m^3
Propellant initial inner wall radius (r_s)	18 mm
Propellant initial thickness (t_s)	14.4 mm
Propellant grain length (L_p)	520 mm
Nozzle throat diameter (d_t)	16 mm
Grain/nozzle convergence length ratio (L_p/L_c)	16

degree and, since the propellant grain motion is of primary importance due to combustion, this is deemed a good option.

The discrete numerical representation of the motor structure is developed using the FE method. Hexahedral elements in a structured grid (i.e., a mesh with a fixed number of elements in the axial, radial, and tangential directions) are used to represent the SRM structural components. The model is developed using the meshing capabilities of ANSYS [9] to create the structural grid. The structured mesh for the reference cylindrical-grain motor is illustrated in Fig. 2(a), where the head-end plate is omitted in the figure for clarity. Structural periodic symmetry can be utilized by the model as shown in Fig. 2(b). The use of symmetry reduces the total degrees-of-freedom for a system and, thus, allows for a significantly refined mesh without affecting the computational performance during a simulation. The structural component has the capability of using a linear-displacement 8-node hexahedral element or a higher-order quadratic-displacement 20-node hexahedral element, consisting of 24- and 60-degrees-of-freedom, respectively [10]. The hexahedral elements are used in this study, providing reduced complexity when passing information between the different model components.

The structural component is developed with some notable assumptions. All of the materials are assumed to behave in a linearly elastic manner. This is accurate for both the aluminium casing and external steel sleeve, since stress levels exhibited are well below yielding limits. However, this is less accurate for the propellant

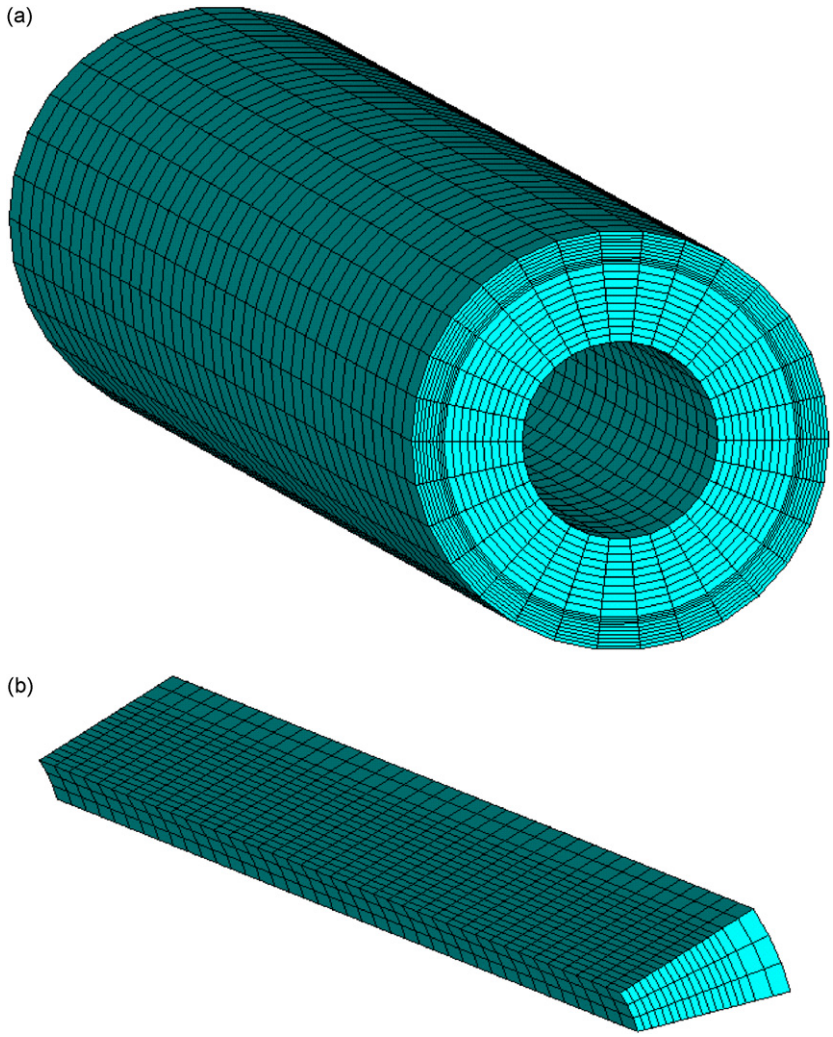

Fig. 2. Three-dimensional mesh (head-end structure omitted in figure for clarity) of (a) full model, (b) 36° periodically symmetric section.

grain, which is typically characterized by nonlinear viscoelastic behaviour (it is common practice in the industry to model the propellant structure as being linearly elastic due to the many uncertainties involved in manufacturing and installing SRM propellants, and due to the lack of physical material data [5]). Furthermore, this assumption has previously proven to provide a feasible structural model as shown by Loncaric et al. [6], which also included the same propellant material properties shown in Table 1. Also, the effects of the core temperature in the motor combustion chamber on the structure are neglected. This approximation is valid since propellant grains typically have low thermal conductivities and, thus, act as insulators to the surrounding structure. The heat penetration zone from the surface of the burning/regressing propellant is typically quite thin. The main effects of temperature are significant in the combustion model and the flow model. Finally, it is assumed that the damping ratio used in the damping model remains constant throughout the simulation. This is assumed mainly for simplification in the structural FE solution, which is typically the case for most structural vibration problems.

The structural component uses Hamilton's principle, which incorporates elemental energy expressions to establish the differential equations of motion. The FE discretization then produces the matrix form of the equations of motion using a typical displacement polynomial expression with corresponding element shape functions [11]; again, assuming a linearly elastic analysis via Hooke's law. The discrete structural FE equations

of motion are given in matrix form as

$$[M]\{\ddot{u}\} + [C]\{\dot{u}\} + [K]\{u\} = \{F\}. \tag{1}$$

The system mass and stiffness matrices are denoted by $[M]$ and $[K]$ (formulations are found in the literature for the presented hexahedral elements [10]), and the system displacement vector is given by $\{u\}$, where the single and double dots over the displacement vector denote derivatives with respect to time for velocity and acceleration, respectively. Note that the displacement based FE formulation of Eq. (1) is used even though the propellant structure has Poisson's ratio of 0.497. Typically, for materials having Poisson's ratio of exactly 0.50 a mixed FE formulation is used to address the incompressible nature of the structure [10]. The propellant material in this study does not exhibit high stresses and as a consequence the strain in the structure is low which results in small displacements limiting any potential incompressible effects. This displacement-based FE formulation has previously proven to work with sufficient accuracy for this type of simulation [6]. Note however that the use of a displacement based FE formulation might result in calculation errors for the structural natural frequencies, and in the future the use of a mixed FE formulation may be preferred.

A spectral damping model (i.e., an equivalent viscous damping model) is used to represent the inherent material damping of the structure. Thus, the system damping matrix, $[C]$, is approximated by the Rayleigh proportional damping method [10],

$$[C] = \alpha[K] + \beta[M]. \tag{2}$$

The damping constants α and β are determined using the system natural frequencies (ω_n) and the specified damping ratio (ζ). The system natural frequencies are obtained using a free vibration analysis, which the algorithm is capable of performing. The system damping ratio is obtained from previous numerical simulations in the literature for this particular SRM [4].

The external force vector $\{F\}$, is determined from the external loading acting on the structure. For a typical SRM, the external structural loading includes surface pressure imparted on the inner propellant surface due to the fluid (high-pressure/temperature gas), pressure imparted on the exterior surface from the atmosphere, and potential body loads (i.e., centripetal acceleration due to motor spinning and axial acceleration due to corresponding flight vehicle motion). For a motor that is in-flight, the external atmospheric pressure may change over time; however, for a motor on a static test stand, the external atmospheric pressure remains constant throughout the simulated firing. Also, the body load per unit volume caused by centripetal acceleration is given by the product of the material density and the local centripetal acceleration magnitude ($\rho r\omega^2$). The body load per unit volume caused by axial acceleration, a_{long}, is given by ρa_{long}. Any acceleration due to gravity is ignored since its magnitude is negligible when compared to the potential centripetal and axial motor accelerations. The final system external force vector is given by

$$\{F\} = \sum_{\text{elements}} \left(\iiint_V [N]^{\mathrm{T}}\{b\}\,\mathrm{d}V \right) + \sum_{\text{surfaces}} \left(\iint_S [N]^{\mathrm{T}}\{p\}\,\mathrm{d}S \right), \tag{3}$$

where $\mathrm{d}V$ and $\mathrm{d}S$ denote volume and surface differentials, respectively. Note that the corresponding element shape function matrix is denoted as $[N]$, the vector $\{b\}$ contains the body load components acting over the structure volume, and the vector $\{p\}$ contains the pressure components acting on the structure surfaces.

There are no point loads acting on the SRM structure, however, there are constraints applied to the structure to restrict any rigid-body motion. For the case of a symmetric structure, the planes of symmetry are restricted from moving in their respective normal directions. With respect to the axial motion, the end-cap at the motor head-end is restricted from moving in the axial direction of the motor (any external motion in the axial direction can be applied to the structure as a body load, which holds true for both static and in-flight simulations). At the nozzle-end of the motor, the end-grain is free to vibrate axially with an applied local pressure at the end-face. The schematic of the boundary constraints for the motor ends is illustrated in Fig. 3. These boundary constraints accurately capture the physical motion of the structure with respect to the core flow.

The structural model is capable of solving a static, free vibration, or dynamic problem. Static problems (i.e., $[K]\{u\} = \{F\}$) are solved using a symmetric, positive-definite decomposition method known as Cholesky factorization [11]. Free vibration problems (i.e., $|[K]-\omega^2[M]| = \{0\}$) are solved using a transformation method

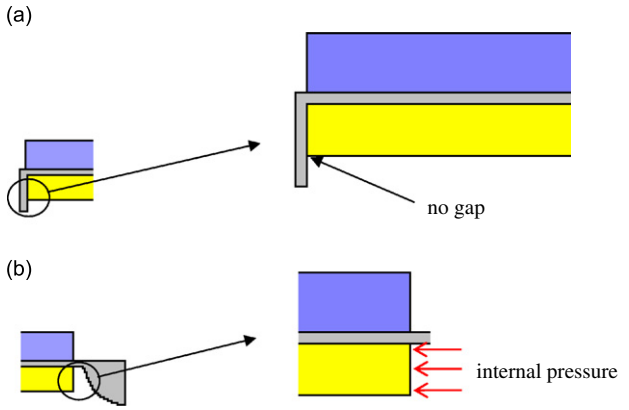

Fig. 3. SRM boundary constraints: (a) head-end and (b) nozzle-end.

known as QL decomposition [11]. For a dynamic analysis (which is typically required for a simulated motor firing), Eq. (1) is solved using a direct time integration method. The algorithm is capable of employing various implicit and explicit methods, such as the Newmark method [10]. The linear matrix equations encountered at each time step of the dynamic solution are solved with the Cholesky factorization method. For the explicit methods, the FE time step, Δt_s, is found by using the CFL condition [10] for a three-dimensional element, such that

$$\Delta t_s \leqslant C_{n_{\mathrm{FE}}} \frac{\Delta L}{\sqrt{E(1-\nu^2)/\rho}}. \tag{4}$$

Here, E is the material elastic modulus, ν the material Poisson's ration, ρ the material density, ΔL the minimum element dimension and the Courant number, $C_{n_{\mathrm{FE}}}$, is set to 0.5. The structural solvers have been optimized for storage and performance, enabling the use of a PC with a Windows environment to perform the various simulation runs.

2.2. IBF component

The IBF model component is the computational fluid dynamics (CFD) algorithm developed to represent the internal core flow in the combustion chamber of the motor, which is depicted as the port in Fig. 1. Rocket core flow problems are difficult to model in comparison to other flow environments. This is mainly due to the fast propagating acoustic disturbances that could potentially result from transient activity affecting the combustion chamber port. Complex numerical solution methods are typically required to minimize the numerical solution noise.

A quasi-one-dimensional flow model is incorporated mainly due to restrictions on the computation time and to keep the model complexity low. For motors with large length-to-diameter ratios (L/D), as in this study, a one-dimensional analysis provides reasonable results, especially in the aft portion of the motor where the flow is fully developed [12]. The flow equations employed are those typically seen for one-dimensional duct flow analysis, with some additional inhomogeneous terms added to account for any mass, energy or momentum addition due to the burning of the propellant (r_b). The equations also include terms for a potential second particulate phase in the flow (mass fraction α_p, particulate density ρ_p, particulate mass m_p, flow velocity u_p, drag force D and heat transfer Q), due to particles added in the propellant grain. The governing compressible quasi-one-dimensional hydrodynamic continuity, momentum and energy flow equations are given as [4]:

$$\frac{\partial \rho}{\partial t} + \frac{\partial(\rho u)}{\partial x} = -\frac{1}{A}\frac{\partial A}{\partial x}\rho u + (1-\alpha_p)\rho_s \frac{4r_b}{d} - \left(\frac{4r_b}{d} + \kappa\right)\rho, \tag{5}$$

$$\frac{\partial(\rho u)}{\partial t}+\frac{\partial}{\partial x}(\rho u^2+p)=-\frac{1}{A}\frac{\partial A}{\partial x}\rho u^2-\left(\frac{4r_b}{d}+\kappa\right)\rho u-\rho a_l-\frac{\rho_p}{m_p}D, \tag{6}$$

$$\frac{\partial(\rho E)}{\partial t}+\frac{\partial}{\partial x}(\rho uE+up)=-\frac{1}{A}\frac{\partial A}{\partial x}(\rho uE+up)-\left(\frac{4r_b}{d}+\kappa\right)\rho E + (1-\alpha_p)\rho_s\frac{4r_b}{d}\left(C_pT_f+\frac{v_w^2}{2}\right)-\rho ua_l-\frac{\rho_p}{m_p}(u_pD+Q). \tag{7}$$

The main flow parameters include the local gas density (ρ), axial flow velocity (u), local static pressure (p), local cross-sectional area (A), local hydraulic diameter (d) and total specific energy (E). Total specific energy is given by $E=(p/(\gamma-1)\rho)+(u^2/2)$, where γ is the gas specific heat ratio. Additional variables in the above three equations include the propellant density (ρ_s), longitudinal acceleration of the gas (a_l), gas heat capacity (C_p), flame temperature (T_f), mass injection velocity (v_w), and the port radial dilatation (κ). Radial dilatation is caused by factors other than the propellant regression (i.e., structural vibrations), and is defined as $\kappa=(1/A)(\partial A/\partial t)$, where t represents time. The spatial variable x is in the axial direction of the motor, beginning from the motor head-end. The control volume of the core flow is discretely represented by nodes along the motor axial direction; there is a finer representation through the nozzle convergence portion in comparison to the flow over the propellant grain. Also, at the motor head-end the flow boundary condition is a fixed wall, whereas at the nozzle-end there is an outflow through the nozzle convergence to the exit plane, which is open to the atmosphere. Note that the port radial dilatation and the longitudinal acceleration of the gas are found from the structural model component.

The unsteady solution of Eqs. (5)–(7) consists of using the random-choice method (RCM), which is an explicit finite-volume method of integrating hyperbolic sets of partial differential equations [13]. A characteristic of the RCM, differentiating it from other conventional finite-volume methods, is the use of a pseudo-random sampling of flow properties at given positions within the flow, in lieu of flow-averaging across an elemental section. The purpose of the sampling is to avoid artificial dissipation of waves in the flow while keeping noise relatively low, a requirement which is prominent in this application due to the inhomogeneous terms in the flow equations and due to the highly nonlinear flow behaviour. Also, a higher-order Riemann approach [4] is used to solve any wave motion caused by the discontinuity at the random position. The random position is located between two neighbouring nodes in the axial direction of the motor and typically experiences a discontinuity in the main flow parameters due to the unsteady transient flow conditions. The inhomogeneous source terms due to grain/nozzle area transition and propellant burning are added to the solution using a second-order method described by Ben-Artzi and Falcovitz [14]. The inhomogeneous source terms due to structural vibrations are added to the Riemann solution through an operator time-splitting technique [15]. The overall solution is solved in space and time using two half-time steps [16].

The CFD algorithm also has the option of solving both quasi-steady and unsteady flow solutions (the quasi-steady flow solution uses a finite difference approximation to solve Eqs. (5)–(7) with a larger time step). Moreover, due to the explicit solver, the time step size for the fluid component is calculated using the CFL condition, such that

$$\Delta t_f \leqslant C_n\frac{\Delta l}{c}. \tag{8}$$

The wave speed is given by $c=u+a$, where a is the sound speed and u is the flow velocity. The IBF Courant number, C_n, is set to 0.5 for all simulated firings, and Δl is the minimum space between fluid nodes. Finally, the fluid algorithm has the capability of simulating the ignition of the motor as well as the onset of a flow disturbance (e.g., an axial shock wave).

2.3. Combustion component

The propellant combustion component utilizes a quasi-steady rapid kinetic rate burning model, which as a result does ignore frequency-dependent combustion effects. The phenomenological burning rate algorithm

consists of three components that influence the overall propellant surface burning rate (r_b): pressure-induced burning, velocity-induced (or erosive) burning and acceleration-induced burning. Pressure-induced burning follows the empirical law of de St. Robert [5],

$$r_p = Cp^n, \tag{9}$$

where n and C are the empirical pressure exponent and the burn rate coefficient, respectively.

The erosive burning model is governed mainly by local convective heat transfer at the propellant burning surface. When the heat flux into the propellant surface is increased, there is a corresponding increase in the local burn rate. The governing equation is given by [4]

$$r_b = r_0 + \frac{h(T_f - T_s)}{\rho_s[C_s(T_s - T_i) - \Delta H_s]}, \tag{10}$$

where r_0 is the base burning rate component including any pressure and acceleration effects, T_s the propellant surface temperature, T_i the propellant initial temperature, C_s the propellant specific heat capacity and ΔH_s the propellant surface heat of reaction. The convective heat transfer coefficient (h) is given by

$$h = \frac{\rho_s r_b C_p}{\exp\left(\dfrac{\rho_s r_b C_p}{h^*}\right) - 1}. \tag{11}$$

The zero-transpiration heat transfer coefficient (h^*) is found via

$$h^* = \frac{k}{d}\,\mathrm{Re}_d\,\mathrm{Pr}^{1/3}\frac{f}{8}. \tag{12}$$

The Reynolds number based on the hydraulic diameter and flow properties is given by $\mathrm{Re}_d = \rho u d/\mu$ (μ is the gas absolute viscosity), the Prandtl number is given by $\mathrm{Pr} = \mu C_p/k$ (k is the gas thermal conductivity), and the Darcy–Weisbach friction factor (f) is given by

$$f^{-1/2} = -2\log_{10}\left(\frac{2.51}{\sqrt{f}\,\mathrm{Re}_d} + \frac{\varepsilon/d}{3.7}\right). \tag{13}$$

The effective propellant surface roughness (ε) is typically estimated for certain propellants.

The acceleration-induced burning can be a significant factor in the augmentation of the local burning rates, as discussed by Sutton and Biblarz [5] and Greatrix [2]. The acceleration-induced burn rate model that is used here combines normal, lateral, and longitudinal acceleration effects, and is given by [4]

$$r_b = \frac{C_p(T_f - T_s)}{C_s(T_s - T_i) - \Delta H_s}\frac{r_b + G_a/\rho_s}{\exp[C_p\delta_0(\rho_s r_b + G_a)/k] - 1}. \tag{14}$$

The reference energy film thickness, δ_0, and the accelerative mass flux, G_a, are both given by

$$\delta_0 = \frac{k}{\rho_s r_0 C_p}\ln\left(1 + \frac{C_p(T_f - T_s)}{C_s(T_s - T_i) - \Delta H_s}\right), \tag{15}$$

$$G_a = \left(\frac{a_n p}{r_b}\frac{\delta_0}{RT_f}\frac{r_0}{r_b}\right)\cos^2\phi_d. \tag{16}$$

The variable R is the specific gas constant, a_n the normal acceleration acting on the burning surface and ϕ_d the augmentation orientation angle

$$\phi_d = \tan^{-1}\left[K\left(\frac{r_0}{r_b}\right)^3\frac{a_l}{a_n}\right]. \tag{17}$$

The term a_l is the vector sum of the lateral and longitudinal acceleration components on the burning surface and the empirical orientation correction factor K is set to 8 [2]. Note that the normal acceleration of the burning surface structure, a_n, is assumed negative in value when directed into the core flow (and resulting in a

compression of the combustion zone), thus, only a negative normal acceleration value augments the burning rate. Also, the lateral and longitudinal acceleration generally reduce the effects of the normal acceleration on the burning rate.

To converge to the overall local burning rate, Eqs. (9)–(17) must be solved iteratively. The existence of nonlinearity in the burning rate equations warrants a nonlinear solution; thus, a Newton–Raphson numerical method is used to solve for the overall local burning rate. This solution occurs for each node along the burning surface of the propellant, based on the local flow parameters and the local acceleration field components. Details of the solution can be found in Ref. [16].

2.4. FSC interface coupling component

The FSC interface coupling component in Fig. 4 is implemented into the numerical model to control the overall simulation, to handle the mesh association between the fluid and structure (i.e., track the interface boundary), and to transfer data between each model component. The simulation is modeled in the time domain, where the three model components are solved separately, each iteration, versus being solved simultaneously in a fully coupled simulation, which is necessary due to the nonlinear nature of the acoustics in the flow [17].

Throughout the simulation each physical component is executed one at a time; then, the interface component extracts the necessary information to be passed to the next component as a boundary condition. The structural component passes the nodal displacements and accelerations of the nodes on the propellant inner burning surface to the interface component, while receiving the interpolated fluid pressure values and the updated regressed FE mesh. The IBF component passes the fluid pressure values and receives the interpolated structural acceleration values, the updated port area and the current burn rate values. Finally, the combustion component passes the burning rate values and receives the interpolated structural acceleration values and the fluid pressure values. Interpolation is necessary every simulation iteration to ensure overall conservation of energy [16].

The interpolated values are determined using a linear interpolation scheme between neighbouring nodes on the interface boundary, which is necessary due to the differences in the alignment of the structural and fluid meshes. Consider interpolating the calculated pressure distribution from the IBF component during a simulation time step, which will be applied as a boundary load to the structure. The fluid and structural grids are not necessarily aligned in space as shown in the one-dimensional schematic of Fig. 5. Consider the spacing between the nodes of the fluid and structural grids in the motor axial direction to be denoted as Δx_{IBF} and Δx_{FE}, respectively. The fluid nodes are defined by $i-1$, i, $i+1$, etc. while the structural nodes are defined by $j-1$, j, $j+1$, etc. The pressure values are known at the fluid nodes, thus to determine the pressure value (λ) at

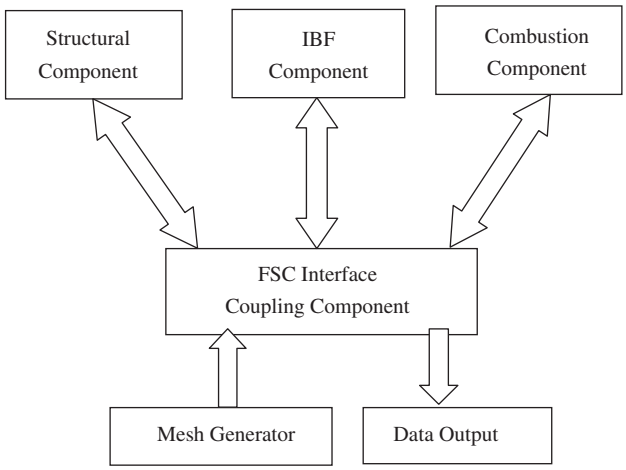

Fig. 4. Overall simulation schematic: component coupling. IBF—internal ballistic flow and FSC—fluid–structure–combustion.

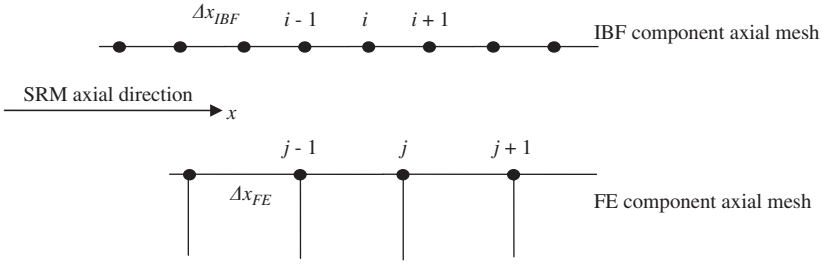

Fig. 5. Fluid–structure grid alignment. SRM—solid rocket motor.

structural node j the following equation can be used which employs a linear interpolation scheme:

$$\lambda_j = \lambda_i - \frac{x_j - x_i}{\Delta x_{\mathrm{IBF}}}(\lambda_i - \lambda_{i+1}). \tag{18}$$

The value λ can represent a general property (such as fluid velocity or local combustion burning rate) that can be interpolated using Eq. (18) and then passed on to the structural component. A similar interpolation scheme can be used if a structural property at the structural grid nodes is known (such as nodal displacement or acceleration) which must be calculated at the fluid grid nodes. This scheme has proven to work well when the fluid and structural grids are refined (i.e., small Δx_{IBF} and Δx_{FE} values). However, if a coarser grid is employed then a higher-order interpolation scheme may be required, which is not the case for this study. This interpolation scheme can also be applied in multidimensions over space as required in a simulation.

The interface component controls the regression of the propellant structure and consequently the change in the control volume of the fluid. The propellant structure in the FE mesh is regressed by the nodes on the interface boundary, which affects the mass, stiffness and damping properties of the structure. The regression of the propellant as it burns depends on the local overall burn rate value and the FE time step size. The FE node regression is in the normal direction of the propellant burning surface with a magnitude and direction given by the vector:

$$\vec{B} = r_b \Delta t_s \hat{n}. \tag{19}$$

For a cylindrical-grain motor, the normal directional vector $\hat{n}$ is simply in the radial direction; however, for general grain geometries, the normal direction may change for various nodes on the propellant burning surface. A schematic of the propellant regression for a cylindrical-grain motor is shown in Fig. 6. Furthermore, the change in the control volume for the fluid is controlled through the port area, A, and thus the hydraulic diameter, d, in Eqs. (5)–(7). The regression of the propellant and the displacement of the propellant burning surface dictate the change in the port area and hydraulic diameter. This is represented numerically for a cylindrical-grain motor as

$$\Delta d = 2(\Delta \mathrm{tr}_b + \Delta u_r). \tag{20}$$

The change in radial displacement (Δu_r) at any motor axial location is determined from the output of the structural component and can be positive or negative. Further details are found in Ref. [16].

The structural and fluid time steps calculated using Eqs. (4) and (8) are related to the overall time step through the interface component. For an implicit structural solver, the structural time step (Δt_s), the fluid time step (Δt_f) and the simulation time step (Δt) are all equivalent (i.e., calculated Δt_f value used). For an explicit structural solver, the simulation time step is set to the maximum of the fluid and structural time steps. For example, if the structural time step is smaller than the fluid time step, then $\Delta t = \Delta t_f$ and the structural solver is employed numerous times between each simulation iteration due to the smaller time-step size. This is done mainly to reduce computation time. The following relationship is used to determine the sub-step number T_{sub},

$$T_{\mathrm{sub}} = \left(\frac{\Delta t_f}{\Delta t_s}\right) + 1. \tag{21}$$

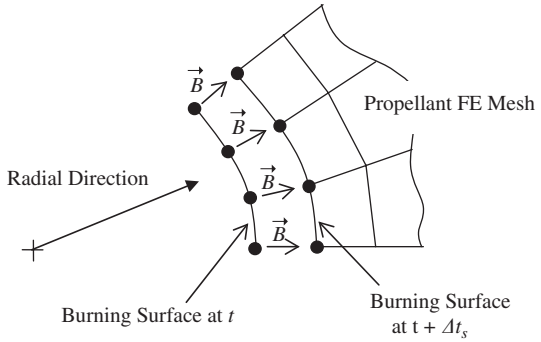

Fig. 6. Propellant regression schematic: normal direction into propellant surface.

The ratio of the fluid and structural time steps is rounded to the nearest integer number. The structural time step is then given by

$$\Delta t_s = \frac{\Delta t_f}{T_{\text{sub}}}. \tag{22}$$

For this study, the fluid time step is typically of the order 10^{-7} s whereas the structural limiting time step is of the order 10^{-8} s.

The interface component ensures that there is conservation of both mass and energy throughout the simulation. This is accomplished through the implementation of a kinematical compatibility at the FSC boundary. For example, the longitudinal acceleration term in the fluid momentum equation (a_l in Eq. (6)) also appears in the acceleration-induced burning rate formulation (a_l in Eq. (17)). This term is calculated from the locally interpolated values of the structural axial propellant acceleration field ($\{\ddot{u}\}$ in Eq. (1)). Thus, for a given point p^* on the interface boundary, the FSC interface component ensures conservation of energy by

$$(a_{l,p^*})_{\text{structure}} = (a_{l,p^*})_{\text{fluid}}. \tag{23}$$

The same is assumed for the displacement and velocity fields at all nodes on the interface boundary. Also, the mass flow from the solid propellant (due to combustion) must be equal to the mass flow into the fluid domain, which is represented mathematically in terms of mass flow per unit area by

$$m_s = m_f = \rho_s r_b. \tag{24}$$

Examination of Eqs. (5)–(7) reveals the mass flow term of Eq. (24), which ensures mass is conserved during the simulation.

A typical simulation controlled by the interface component is depicted in Fig. 7. It begins with the input of the FE mesh and the initialization of all the physical components (e.g., motor ignition). Then, the time steps are calculated and synchronized and the unsteady flow solution begins. The initial structural transients and the fluid pressure are input to the combustion component for burning rate calculation. The fluid pressure values are interpolated and applied to the structural model, and the structural solution is initiated. The structural displacement and acceleration values are interpolated for both the IBF and combustion components for the next iteration. The FE mesh is regressed, the control volume for the fluid is updated and the simulation iterations continue until a predetermined simulation time or until a manual simulation freeze. Also, at the end of each simulation time step, any specified data (for example, the nodal accelerations, fluid pressures, or burn rate) are output.

3. Results and discussion

In this section, results are presented to illustrate and validate the simulation and coupling capabilities of the numerical model. The flow and propellant burning characteristics for the cylindrical-grain SRM used for the simulations are presented in Table 2, with data typical for a non-aluminized ammonium perchlorate/

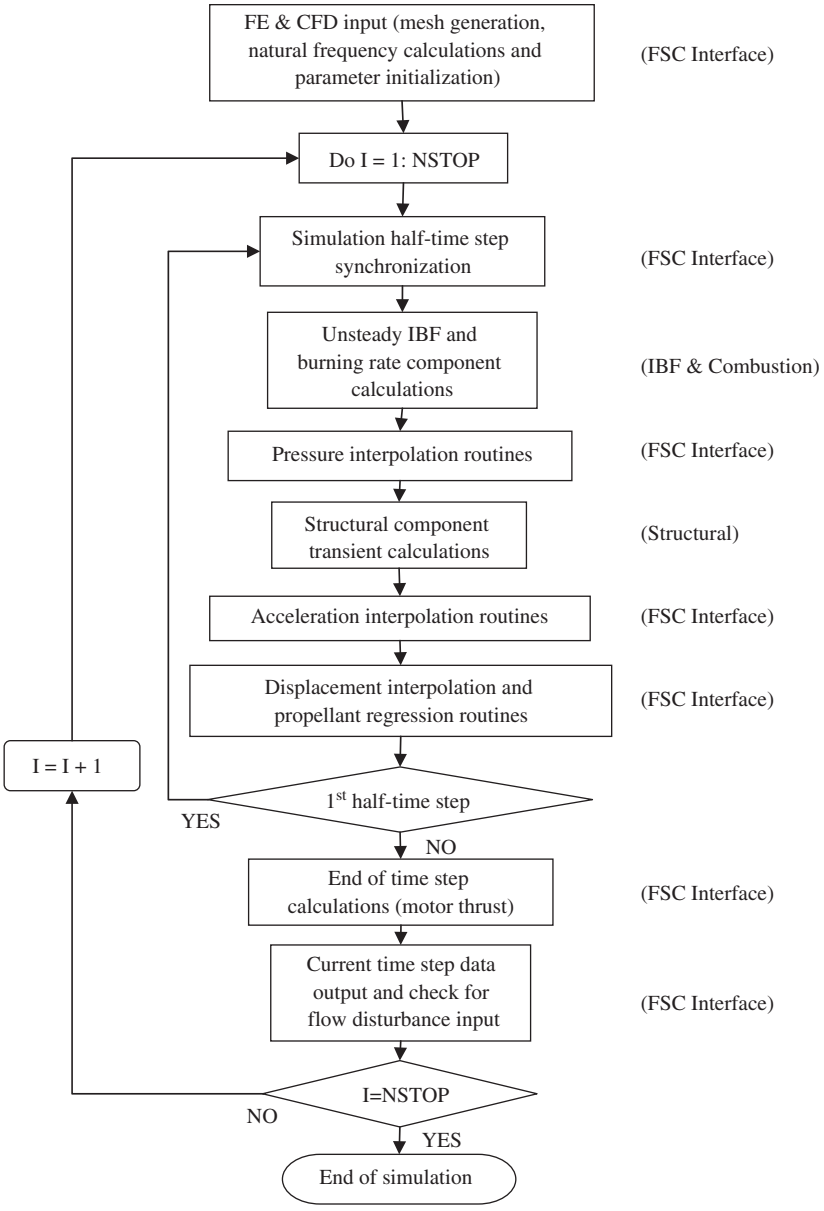

Fig. 7. Simulation flow chart. FSC—fluid–strucutre–combustion and IBF—internal ballistic flow.

hydroxyl-terminated polybutadiene propellant. Note that the pressure-dependent burning rate parameters (C and n) from the empirical relationship are combined in Table 2. The FE structural mesh consists of 14,400 8-node hexahedral elements, while the fluid mesh consists of 260 axial nodes. The structural damping ratio is set to 0.35, unless specified otherwise, while the calculated fundamental natural frequency and the radial response frequency are 1790 and 15,950 Hz, respectively. Also, the structural solver used here is an explicit version of the Newmark time integration method [10].

The first simulation is a cold-flow case (i.e., no propellant regression), where the intention is to test the capabilities of the structural solvers and the structural damping model. The result of a 10.5-MPa step pressure pulse imposed on the structure is illustrated in Fig. 8(a) by the predicted head-end radial displacement–time profiles for the propellant surface and the steel sleeve outer surface. In this simulation, the damping ratio is set to 0.1. The results correlate well with the predicted results of Greatrix and Kudriavtsev [18] using a

Table 2
Reference cylindrical SRM flow and combustion properties

Pressure-dependent burning rate (r_p)	$0.05\,[p(\text{kPa})]^{0.35}$ cm/s
Propellant specific heat (C_s)	1500 J/kg K
Propellant flame temperature (T_f)	3000 K
Propellant surface temperature (T_s)	1000 K
Initial propellant temperature (T_i)	294 K
Propellant surface roughness (ε)	400 μm
Gas specific heat (C_p)	2000 J/kg K
Gas Prandtl number (Pr)	0.828
Specific gas constant (R)	320 J/kg-K
Gas thermal conductivity (k)	0.195 W/m K
Gas absolute viscosity (μ)	8.07×10^{-5} kg/m s
Gas specific heat ratio (γ)	1.2
Particle mass fraction (α_p)	0%

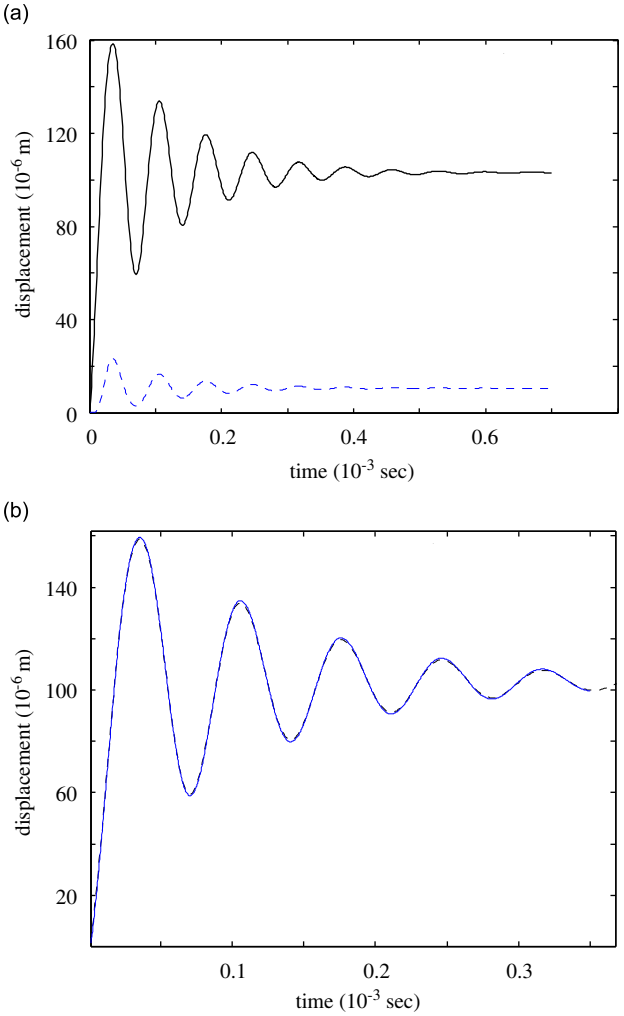

Fig. 8. Radial displacement, motor head-end: (a) — propellant inner surface, --- steel outer surface, (b) — propellant inner surface (current model), --- propellant inner surface (CFD ACE software).

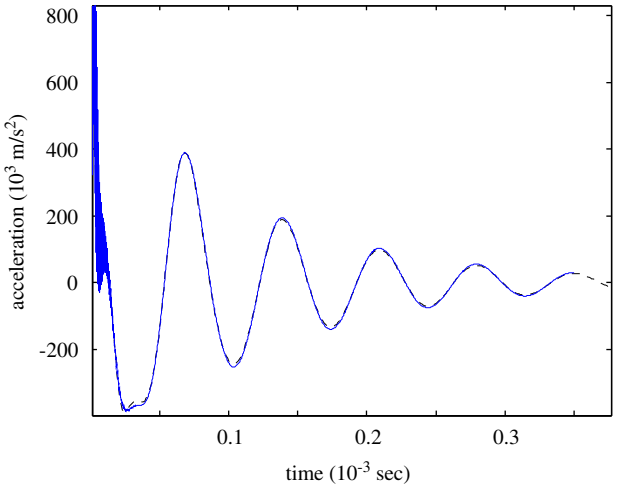

Fig. 9. Propellant radial acceleration, motor head-end: --- CFD ACE software predictions, — current model.

commercial fluid–structure package, CFD ACE+. The damped response frequency is approximately 15 kHz (for both the propellant and the steel), which also correlates well to the same literature. The propellant radial displacement results of both simulations are superimposed in Fig. 8(b). Also, the predicted head-end propellant radial acceleration–time profiles for each simulation are also plotted together as shown in Fig. 9. There is minimal difference between the two simulations, which is a validation of the accuracy of the structural model solution procedure. Specifically, the accuracy of the acceleration profile proves to be crucial for the hot-flow simulations since, as mentioned, the structural acceleration has a direct impact on the combustion of the propellant.

The second simulation is a hot-flow firing of the cylindrical-grain SRM, including all three physical model components. The intention of this simulation is to verify the coupling capabilities of the overall simulation model and, specifically, the performance of the FSC interface coupling component. The same reference cylindrical-grain motor is used, which is subjected to a 1.2-MPa overpressure pulse (i.e., a shock wave) in the core flow initiated at a later time in the simulation, after the solution has settled at an equilibrium point. At this point in the simulation, the regression routines have sufficiently followed the movement of the burning surface. The predicted mid-grain pressure–time profile for the initial passing and reflection of the pressure pulse is shown in Fig. 10(a), while the predicted mid-grain propellant inner surface radial displacement–time profile is illustrated in Fig. 10(b). The plots show good correlation between the applied pressure and the radial structural response, where the peaks caused by the shock front are coinciding in simulation time, which is not surprising. More importantly, the acoustic oscillations after the shock has passed the motor mid-grain have a frequency that is approximately equal to the radial structural response frequency. This was found in many experimental motor firings [4] and shows the significant capability of the numerical model to simulate an SRM firing.

The predicted mid-grain propellant radial acceleration-, longitudinal acceleration- and burning rate–time profiles are included in Fig. 11(a)–(c), respectively (again for the initial passing and reflection of the pressure pulse). The transient acceleration field directly augments the burning rate, as presented by Eqs. (14)–(17), which is evident through the radial acceleration peaks and burning rate peaks in the respective plots. Recall that only the negative radial acceleration values augment the burning rate. The higher negative radial acceleration values have a greater effect on the burning rate, which is a characteristic of the accelerative mass flux term (i.e., G_a in Eq. (16)). Also, the longitudinal acceleration peaks of Fig. 11(b) are quite large relative to the radial acceleration peaks (the propellant tends to accelerate axially in the direction of lower pressure), which was also seen in a cold-flow study by Greatrix [19]. In this simulation, the negative radial acceleration peaks and the longitudinal acceleration peaks are in phase, thus the longitudinal acceleration reduces the effects of the radial acceleration on the burn rate. The steel sleeve outer surface radial acceleration–time profile at the motor mid-grain is also shown in Fig. 11(d). The peaks are significantly

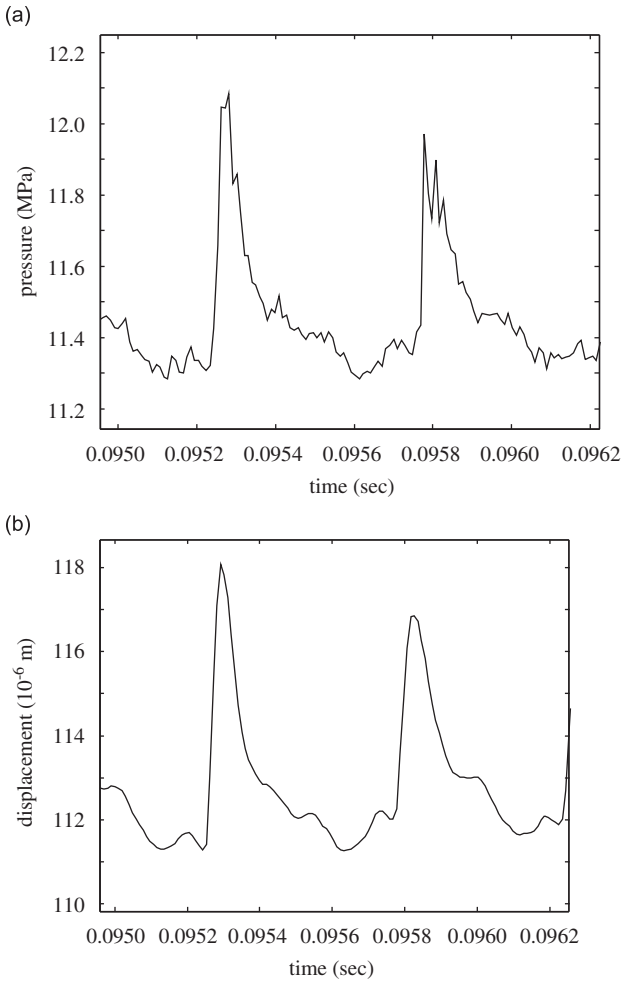

Fig. 10. Response to shock wave, mid-grain (a) pressure–time profile and (b) propellant radial displacement–time profile.

lower in magnitude compared with the propellant radial acceleration peaks and are in phase, as is expected.

Finally, Fig. 12 shows plots of the pressure–time profiles at the motor head-end, mid-grain and nozzle-end-grain. The shock wave initially passes the head-end and mid-grain of the motor, reflects off the nozzle structure, and the reflected wave travels up towards the head-end of the motor port cavity. The ability of the IBF model component to converge to a solution with nonlinear flow behaviour is illustrated. Also, since the reflected shock wave is similar in strength to the incident shock wave, the energy input into the acoustic system due to an increase in the propellant burn rate is clearly shown. Note, there are energy dissipating mechanisms in SRMs (i.e., the structural damping), thus energy must be input into the acoustic system for a reflected wave to have a comparable magnitude to the incident wave. The propellant radial acceleration oscillations (after the shock wave has passed; in Fig. 11(a)) directly affect the burn rate, which clearly influence the acoustic oscillations of Fig. 12, further reinforcing that the added acoustic energy is a result of the increased propellant burn rate.

The experimental results of Greatrix and Harris [4] allow for an excellent basis for comparing and validating the numerically simulated motor firings and the numerical model motor characteristics defined in Tables 1 and 2. The experimental motor firings were performed using the same cylindrical-grain SRM presented in this study, which included employing a similar pulse-triggered pressure disturbance introduced into the motor core flow at a predetermined time. The intention of the experiment was to determine the influence of the dynamic

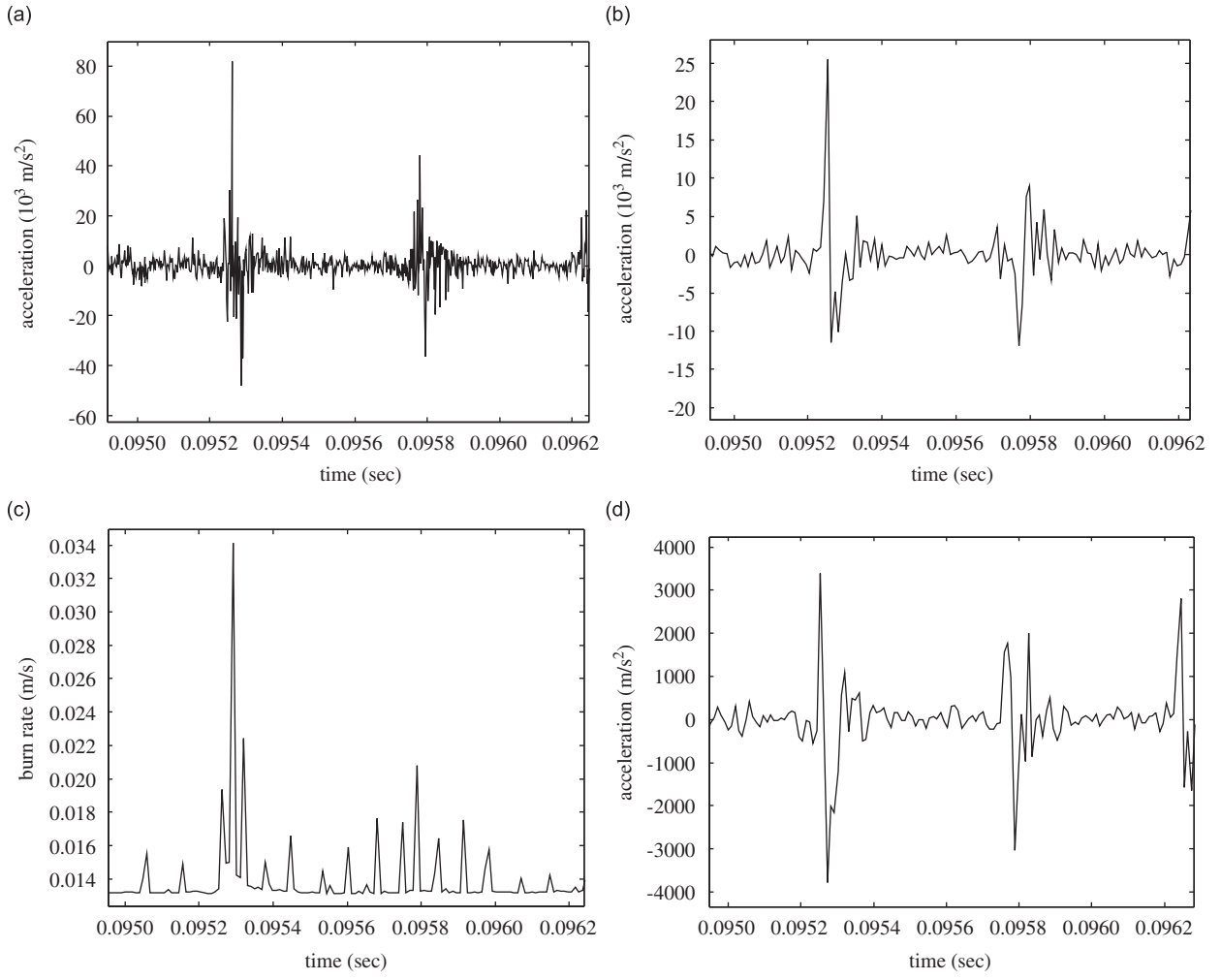

Fig. 11. Response to shock wave, mid-grain time profile of (a) propellant radial acceleration, (b) propellant longitudinal acceleration, (c) burning rate, and (d) steel sleeve radial acceleration.

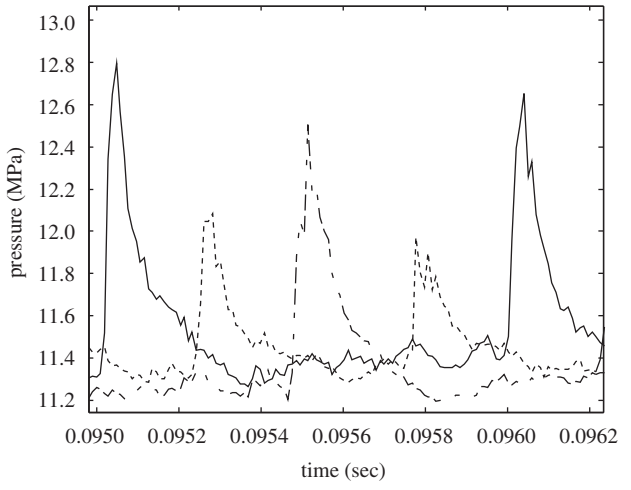

Fig. 12. Comparison of pressure profiles for various motor locations: — head-end, - - - mid-grain, —·— nozzle-end.

motor structure on the internal chamber flow and the propellant combustion, while evaluating the effects on the performance of the sleeved cylindrical-grain SRM. The instrumentation used during the experimental motor firings included both low- and high-frequency pressure transducers at the motor head-end to measure the flow pressure, and accelerometers on the outer steel static-test sleeve to measure structural acceleration.

The experimental plot of the motor chamber head-end pressure–time profile for two cycles of the pressure pulse is shown in Fig. 13. The trend of the shock-front is similar to that found through the numerical simulations (refer to Fig. 10(a)). Also, when comparing the experimental plot to the head-end plot of Fig. 12, the accuracy of the numerical simulation is revealed. The magnitudes of the pressure waves at their peak strength in both plots are approximately 2 MPa from base to peak. Note that the experimental and numerical plots have different base pressures, which is attributed to the shifted simulation times (the experimental plot displays a later time in the motor firing; this is of little importance since the trend in the pressure profile is what ensures the accuracy in the numerical simulation). Moreover, the energy balance in the motor is evident in the experimental pressure plot since the second pressure peak has a comparable magnitude to the first pressure peak. This is the case with the numerical head-end pressure plot, which further illustrates that the energy input into the system is equivalent to the energy dissipated by the system. Also, the frequency of the shock-front in

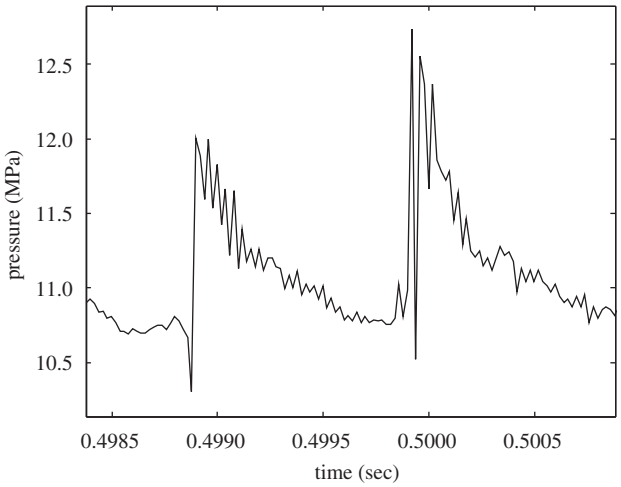

Fig. 13. Experimental head-end pressure–time profile (Defence Research Establishment Valcartier, Ref. [4]).

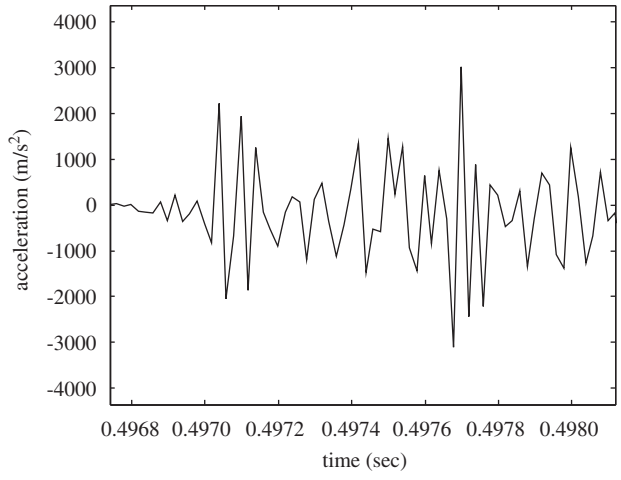

Fig. 14. Experimental mid-grain steel sleeve radial acceleration (Defence Research Establishment Valcartier, Ref. [4]).

both the experimental motor firing and the numerical simulation is approximately 1 kHz (i.e., frequency = 1 cycle/0.001 s), which illustrates the accuracy of the acoustic disturbance development in the simulation.

The experimental plot of the mid-grain outer steel sleeve radial acceleration for two cycles of the pressure pulse is shown in Fig. 14. The magnitude of the acceleration peaks (approximately $\pm 3000\,\mathrm{m/s^2}$) are comparable to the levels of the numerical simulation seen in Fig. 11(d), which further validates the structural dynamics of the numerical model. The experimental oscillations between the radial acceleration peaks are substantial and have an oscillation frequency of approximately 20 kHz, similar to that of Fig. 11(d). The magnitudes of these oscillations are greater in the experimental motor firing and can be attributed to the sensitivity of the instrumentation and possibly the structural damping used in the model.

4. Concluding remarks

The present model simulated the FSC interaction in an SRM. Improvements to previous simulation models have also been presented and demonstrated by the present model simulation results. The results have illustrated the accuracy of coupling the three physical model components through the FSC interface coupling component. Comparisons of the numerical simulation results with the experimental results involving the actual operating performance of a similar motor show good correlation and yield a better physical understanding of the FSC interaction inherent to SRMs. The present model provides an accurate solution in a relatively short period of time on a simple PC computational platform. Moreover, the current model can be used for simulating various motor transient situations, such as combustion instability analysis or for pressure overshoot analysis after motor ignition, where acoustic and structural transient behaviour is heavily coupled to the propellant combustion process (for either smaller scale or larger scale motors).

Some recommendations for future efforts are to include the addition of nonlinear viscoelastic material behaviour and/or large deformation capabilities for the propellant structural model, a variable structural damping ratio for simulated motor firings with a longer simulation time, and the inclusion of a three-dimensional flow model which may account for re-circulating flow and potential transverse wave effects in the motor core. Also, inclusion of a frequency-dependent combustion model may provide additional increased accuracy in the simulation. Recommendations for future experimental motor firings would include implementing a means for measuring the propellant oscillation behaviour with accuracy. Current limitations involved with physical SRM firings restrict any further comparison between the physical motor operation and the numerical simulation results. An experimental measurement of the propellant radial and longitudinal acceleration fields would be beneficial towards further validation of the numerical simulation. Also, cold flow motor firings with an inert propellant may also yield some insight on the structural dynamics of the propellant, as would structural testing of propellant specimens.

Acknowledgements

The authors would like to thank the Natural Sciences and Engineering Research Council of Canada (NSERC) for funding in support of this project.

References

[1] J.J. Gottlieb, D.R. Greatrix, Numerical study of the effects of longitudinal acceleration on solid rocket motor internal ballistics, *Journal of Fluids Engineering* 114 (1992) 404–410.

[2] D.R. Greatrix, Parametric analysis of combined acceleration effects on solid propellant combustion, *Canadian Aeronautics and Space Journal* 40 (1994) 68–73.

[3] D.R. Greatrix, Combined structural oscillation effects on solid rocket internal ballistics, *AIAA/ASME/SAE/ASEE 35th Joint Propulsion Conference*, Los Angeles, CA, USA, June 1999, AIAA Paper No. 99-2509.

[4] D.R. Greatrix, P.G. Harris, Structural vibration considerations for solid rocket internal ballistics modeling, *AIAA/ASME/SAE/ASEE 36th Joint Propulsion Conference*, Huntsville, AL, USA, AIAA Paper No. 2000-3804, July 2000.

[5] G.P. Sutton, O. Biblarz, *Rocket Propulsion Elements*, Wiley, New York, 2001.

[6] S. Loncaric, D.R. Greatrix, Z. Fawaz, Star-grain rocket motor—nonsteady internal ballistics, *Aerospace Science and Technology Journal* 8 (2004) 47–55.

[7] I.D. Parsons, P. Alavilli, A. Namazifard, X. Jiao, A. Acharya, Fluid–structure interaction through a non-material interface: simulations of solid rocket motors, *CDROM Proceedings of the 14th ASCE Engineering Mechanics Conference (EM2000)*, Austin, TX, USA, May 2000.
[8] J. Majdalani, G.A. Flandro, Some recent developments in rocket core dynamics, *AIAA/ASME/SAE/ASEE 39th Joint Propulsion Conference*, Huntsville, AL, USA, AIAA Paper No. 2003-5112, July 2003.
[9] ANSYS Finite Element Program Version 5.5 User's Manual, ANSYS Inc., Houston, 1998.
[10] R.D. Cook, D.S. Malkus, M.E. Plesha, *Concepts and Applications of Finite Element Analysis*, Wiley, New York, 1989.
[11] M. Petyt, *Introduction to Finite Element Vibration Analysis*, Cambridge University Press, Cambridge, UK, 1990.
[12] D.R. Greatrix, J.J. Gottlieb, Erosive burning model for composite-propellant rocket motors with large length-to-diameter ratios, *Canadian Aeronautics and Space Journal* 33 (1987) 133–142.
[13] J. Glimm, Solution in the large for nonlinear hyperbolic systems of equations, *Communications on Pure and Applied Mathematics* 18 (1965) 697–715.
[14] M. Ben-Artzi, J. Falcovitz, An upwind second-order scheme for compressible duct flows, *SIAM Journal on Scientific and Statistical Computing* 7 (1986) 744–768.
[15] G.A. Sod, A numerical study of a converging cylindrical shock, *Journal of Fluid Mechanics* 83 (1977) 785–794.
[16] J. Montesano, Fluid–Structure Interaction Considerations for Solid Rocket Motor Internal Ballistics Modeling, MSc Thesis, Ryerson University, 2005.
[17] P. Leyland, *Fully Coupled Fluid–Structure Algorithms: Fluid–Structure Interaction*, Kogan Science, London, 2003.
[18] D.R. Greatrix, V. Kudriavtsev, Modeling of structural vibration for motor chamber internal flow studies, *ASME Pressure Vessels and Piping Conference*, Vancouver, Canada, August 2002, pp. 95–101.
[19] D.R. Greatrix, Fluid–structure interactions in solid rocket, *Fiftieth Annual Canadian Aeronautics and Space Institute Conference: 9th Aerodynamics Symposium*, Montreal, Canada, Canadian Aeronautics and Space Institute Paper No. 272, April 2003.